Astronomy Letters, Vol. 25, No. 9, 1999, pp. 555–568. Translated from Pis'ma v Astronomicheskii Zhurnal, Vol. 25, No. 9, 1999, pp. 643–657.

Jet Structure in the Quasars 3C 345 and 1803+784

L. I. Matveyenko[1] and A. I. Witzel[2]

[1] *Space Research Institute, Russian Academy of Sciences, ul. Profsoyuznaya 84/32, Moscow, 117810 Russia*

[2] *Max-Planck-Institut für Radioastronomie, Auf dem Huegel 69, Bonn, 53121 Germany*

Received April 1, 1999

Abstract—The fine structure of the AGN objects 3C 345 and 1803+784 is studied. Their jets are shown to have conical helical structures. The helix diameter and pitch are proportional to the distance from the nucleus (injector). The helix axis is curved. This structure is attributable to a short- and long-period precession of the accretion-disk rotation axis. The jet is cocooned in a thin layer of thermal plasma with $l \approx 0.01$ pc, whose transparency increases as one recedes from the nucleus. The thermal-electron density in the cocoon wall near the nuclear region is $N_e \geq 10^6$ cm^{-3}. The nuclear activity causes the cocoon transparency to change, which results in a low-frequency variability of radio emission from the quasars and in a change of polarization parameters. The cocoon transparency determines the visible part of the jet and "displaces" the nucleus from the injector. The nucleus is a compact, bright region of the jet, whose brightness temperature does not exceed the Compton limit. The jet spectrum exhibits a low-frequency cutoff. The cutoff frequency in the spectrum of the nuclear region lies at short centimeter wavelengths and shifts to lower frequencies as one recedes from the injector. The low-frequency spectral index is steep and reaches $\alpha = 4$, which is attributable to additional absorption of synchrotron radiation in the cocoon wall. The high-frequency spectral index is typical of optically thin sources and is $\alpha \approx -1.5$ at large distances from the nucleus.

INTRODUCTION

The quasar 3C 345 and the source 1803+784 (a BL Lac object) are typical objects with active galactic nuclei (AGNs). They have similar redshifts—$z = 0.595$ and 0.68, respectively—which correspond to distances of 2500 and 2700 Mpc to them. In this case, 1 mas corresponds to ~4 and ~5 pc, respectively. Their optical and radio spectral characteristics are identical, while their structure is typical of most AGN objects and consists of a nucleus and a one-sided jet. The nuclear radio emission dominates at high frequencies (in the millimeter and centimeter bands).

The enhanced nuclear activity manifests itself as radio bursts up to several months in duration (Bregman *et al.* 1986). Bursts first show up in the millimeter band and then shift to lower frequencies, while their radio flux density decreases. High-frequency radio bursts are attributable to synchrotron radiation from compact, dense clouds of relativistic plasma which are occasionally expelled from the nucleus. The apparent cloud velocity exceeds the speed of light (Cohen *et al.* 1976).

The radio-emission variations at low frequencies (decimeter wavelengths) are random (fluctuations) in nature (Padrielli 1982). The amplitude and duration of the low-frequency variability suggest brightness temperatures $T_b \approx 10^{16}$ K for the emitting region (Gopal-Krishna *et al.* 1984), which is well above the Compton limit $T_c = 10^{12}$ K (Kellermann and Pauliny-Toth 1969).

A large amount of observational data on AGN objects has been accumulated to date. An analysis of the data for 3C 345 and 1803+784, their fine structure, kinematics, distribution of radio spectral indices, the causes of the low-frequency "cutoff", and the physical processes in them are the subject of this study.

THE QUASAR 3C 345

The fine structure of 3C 345 has been investigated in a wide range of radio wavelengths, from millimeter to decimeter wavelengths inclusive (Zensus 1991; Zensus *et al.* 1995; Bååth *et al.* 1992; Krichbaum *et al.* 1993; Unwin and Wehrle 1992; Rantakyrö *et al.* 1992, 1995; Matveenko *et al.* 1992, 1996; Lobanov and Zensus 1993).

One of the difficulties in studying the fine structure of AGN objects in detail is the identification of its components. The component positions depend both on frequency and on time. A bright, compact source—the nucleus—shows up clearly at high frequencies. However, determination of the nucleus position involves difficulties even at long centimeter, let alone decimeter, wavelengths.

Several characteristic features of the jet—the presence of transverse structures which are observed at centimeter-decimeter wavelengths—allow us to identify them and to determine the nucleus position. The nucleus and transverse structures clearly show up at $\lambda = 6$ cm

1063-7737/99/2509-0555$15.00 © 1999 МАИК "Наука/Interperiodica"

in Fig. 1a (Unwin and Wehrle 1992). The radio isophotes at $\lambda = 18$ and 49 cm exhibit similar transverse structures, which made it possible to determine the nucleus position. The transverse structures lie at angular distances of approximately 5, 15, 30, 55, and 140 mas from the nucleus (Matveenko *et al.* 1996). Their positions are stable enough and depend on frequency only slightly. They are probably associated with shock waves (Readhead *et al.* 1978; Matveenko *et al.* 1992; Biretta *et al.* 1986; Rantakyrö *et al.* 1992; Unwin and Wehrle 1992). The nucleus was found to be 16 mas east (PA = 95°) of the brightest compact region at $\lambda = 49$ cm. Its brightness temperature is $T_{peak} \approx 10^{12}$ K and essentially matches the Compton limit. Thus, the synchrotron nature of the low-frequency radio emission from the compact region was confirmed, and its optical depth was found to be fairly large.

The apparent brightness temperature of the nucleus itself at 49 cm is considerably lower and does not exceed $T_b \leq 0.003 T_{peak}$. The optical depth of the relativistic plasma in the nucleus (injector) must be larger than that in the above region. As before, its low-frequency radio emission from the injector region is probably determined by the synchrotron mechanism, while the brightness temperature matches the Compton limit. At the same time, the observed low temperature of the nucleus can be explained by a substantial (more than a factor of 300) absorption of its radio emission at 49 cm. The absorption of radio emission by an ionized medium is proportional to e^{τ}, while the optical depth is $\tau \sim \lambda^{2.1}$. Hence, the absorption is moderate at 6 cm and does not exceed 4. For this reason, the nucleus clearly stands out on centimeter-wavelength maps as a bright, compact component (Fig. 1a).

The quasar structure at millimeter wavelengths is presented in several papers (Zensus 1991; Zensus *et al.* 1995; Bååth *et al.* 1992; Krichbaum *et al.* 1993). An analysis of the fine structure of the nuclear region indicates that compact components (C_1–C_7) were ejected at the epoch 1983.0–1990.5 in a direction of PA ~ –105°. The component injection direction gradually changed within ~60° and was repeated in approximately 7 years. In this case, the ejected components receded from the injector along a conical helical trajectory. The helix pitch (T) and diameter ($\varnothing$) are proportional to the distance from the nucleus ~(ρ). This structure is traceable up to distances of ~10 pc, which are determined by the lifetimes of the compact components and by the change in their optical depth (visibility).

The jet structure follows and, probably, coincides with the helical trajectory of the compact components. The helical jet structure is particularly clear in a gray-level image (Fig. 1b) (Unwin and Wehrle 1992). This suggests a common mechanism of their formation. Figures 1c–1i show isophotes of 3C 345 at 1.35–49 cm. As we see from the captions to the figures, the isophotal levels correspond to a nonlinear scale. This is done for a better visibility of structures with a low brightness temperature. However, such an "extension" of the visibility range "blurs" the perception of the main jet structure. The curve which is drawn over the "trough" of peak emission along the jet remedies this drawback and delineates the spiral structure (it is shown in the figures). Since the optical depth of the relativistic-plasma flow decreases with increasing distance from the nucleus, at large distances the helical structure shows up more clearly at low frequencies. We used these data to determine the helix parameters (see Fig. 2). To a first approximation, the diameter of the helical jet ($\varnothing$) and its pitch (T), as with the trajectory of the compact components, are proportional to the distance ρ from the nucleus. The helix diameter (in mas) is $\sim 0.55\rho^{0.9}$. The helix pitch $T = 0.15\rho$ up to $\rho = 400$ mas, and its increase slows down at large distances ($T = 4.6\rho^{0.4}$).

The helical structure of the jet can be explained by a precession of the rotation axis of the accretion disk, the injector of relativistic plasma. The relativistic plasma is injected along the rotation axis. The rotation period of the accretion disk can be determined from the relation $\omega R \approx 0.1$ c, where ω is its angular velocity and its radius is $R \approx 10^{15}$ cm (Begelmann *et al.* 1984). It thus follows that the rotation period is $T \approx 2 \times 10^6$ s or ~14 rotations per year. The injector rotation therefore leads to a twisting of the plasma flow.

The twisted flow of relativistic plasma moves at a relativistic velocity, generates a magnetic field, and is self-focused into a jet (Bisnovatyi-Kogan *et al.* 1969; Shakura *et al.* 1973; Begelmann *et al.* 1984; Lovelace *et al.* 1991). This process produces a channel, a magnetic tube along which the flow of relativistic plasma and occasionally ejected dense plasma knots (compact components) move. Since the accretion disk (the injector) precesses, both the magnetic tube and the enclosed flow of relativistic plasma wind themselves around the rotation axis to produce a helical structure. As follows from observations, the precession angle is ~60°, and the precession period corresponds to one rotation in 7 years.

The jet axis is curved. Its orientation changes from –105° near the injector to –30° at a distance of 3″ from the nucleus (Browne *et al.* 1982; Matveenko *et al.* 1992). The curvature of the helix axis is probably determined by the long-period precession velocity of the accretion-disk rotation axis. The precession angle is ≥75°. The position angle φ of the jet axis varies with distance ρ as $\varphi \sim \rho^{1/3}$. This suggests an increase in the long-period precession velocity with time or is possibly attributable to a change in the projection of the axis onto the plane of the sky.

Let us consider the distribution of brightness temperature (radio flux density per beam, F/Ω, in Jy mas^{-2}) along the helix at various wavelengths (see Figs. 1c–1h). These brightness distributions (in Jy beam^{-1}) were obtained with different angular resolutions, $\Omega = Q * \Theta$, and are given in the captions to the figures. To compare these data, they must be reduced to a single angular res-

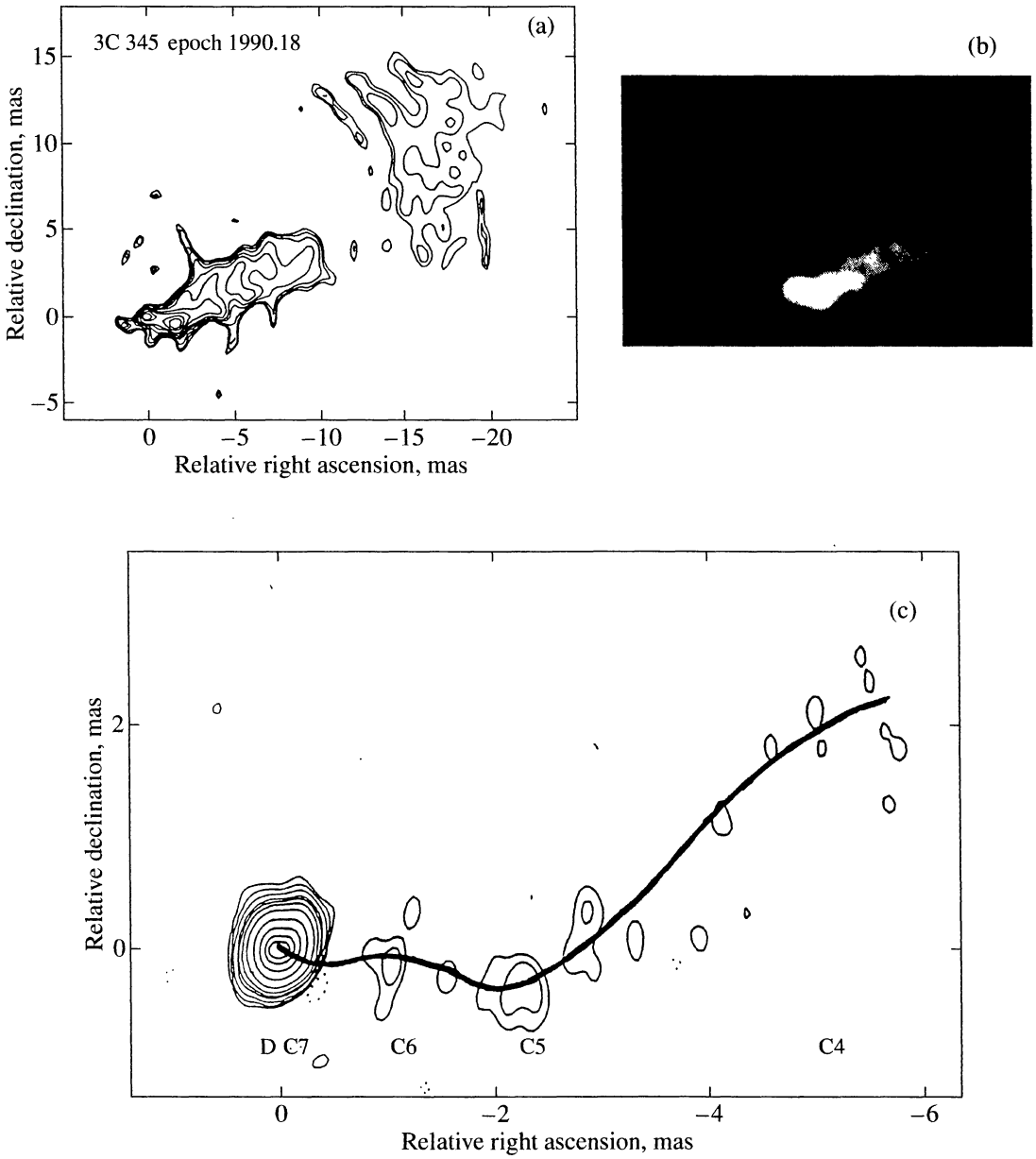

Fig. 1. (a) Radio image of the quasar 3C 345 at various frequencies: $\lambda = 6$ cm, epoch 1990.18, the isophotal levels are (2.5, 5, 10, 25, 50, 100, 500, 1200, 2500) mJy mas^{-2}; the peak brightness is 4.79 Jy mas^{-2} (Unwin and Wehrle 1992). (b) A gray-level image of the quasar. (c) $f = 22$ GHz, epoch June 12, 1992, the isophotal levels are (–0.25, 0.25, 0.50, 1.0, 2.0, 3.0, 5.0, 10.0, 25.0, 50.0, 75.0, 90.0)%; the peak brightness is 4.86 Jy beam^{-1}; a synthesized beam of 0.35×0.17 mas^2; PA = –11.°4 (Zensus 1991). (d) $f = 8.4$ GHz, epoch Sep. 16, 1992, the isophotal levels are (–0.1, 0.1, 0.2, 0.3, 0.5, 1.0, 2.0, 3.0, 5.0, 10.0, 25.0, 50.0, 75.0, 90.0)%; the peak brightness is 6.9 Jy beam^{-1}; a -0.89×0.45-mas^2 beam; PA = –8.°5 (Zensus 1991). (e) $f = 5.0$ GHz, epoch 1989.28, the isophotal levels are (–2, 2, 4, 10, 20, 40, 100, 200, 400, 800, 1600) mJy beam^{-1}; the peak brightness is 2.97 Jy beam^{-1}; a synthesized 1.1-mas^2 beam (Unwin and Wehrle 1992). (f) $f = 5.0$ GHz, epoch June 4, 1992, the isophotal levels are (–0.06, 0.06, 0.13, 0.25, 0.50, 1.0, 2.0, 3.0, 5.0, 10.0, 25.0, 50.0, 75.0, 90.0)%; the peak brightness is 3.07 Jy beam^{-1}; a 1.43×0.83-mas^2 beam; PA = –5.°7 (Zensus 1991). (g) $f = 1.6$ GHz, epoch Apr. 9, 1985, the isophotal levels are (–0.05, 0.03, 0.05, 0.07, 0.10, 0.15, 0.20, 0.25, 0.30, 0.40, 0.50, 0.70, 1.0, 1.5, 2.0, 2.5, 3.0, 4.0, 5.0, 7.0, 10.0, 15.0, 20.0, 25.0, 30.0, 40.0, 50.0, 70.0, 90.0) mJy beam^{-1}; the peak brightness is 3.97 Jy beam^{-1}; a 3×3-mas^2 beam (Rantakyrö *et al.* 1992). (h) $f = 0.6$ GHz, epoch 1986.8, the isophotal levels are (–0.25, 0.25, 0.50, 1.0, 2.5, 5.0, 10.0, 20.0, 40.0, 50.0, 60.0, 70.0, 80.0, 90.0)%; the peak brightness is 3.2 Jy beam^{-1}; a 10×10-mas^2 beam; PA = –11.°4 (Matveenko *et al.* 1996). (i) $f = 0.6$ GHz, epoch 1986.8, the isophotal levels are (0.05, 0.10, 0.25, 0.50, 1.0, 2.5, 5.0, 10.0, 20.0, 40.0, 50.0, 60.0, 70.0, 80.0, 90.0)%; the peak brightness is 4.0 Jy beam^{-1}; a 120×120-mas^2 beam; PA = –11.°4 (Matveenko *et al.* 1996).

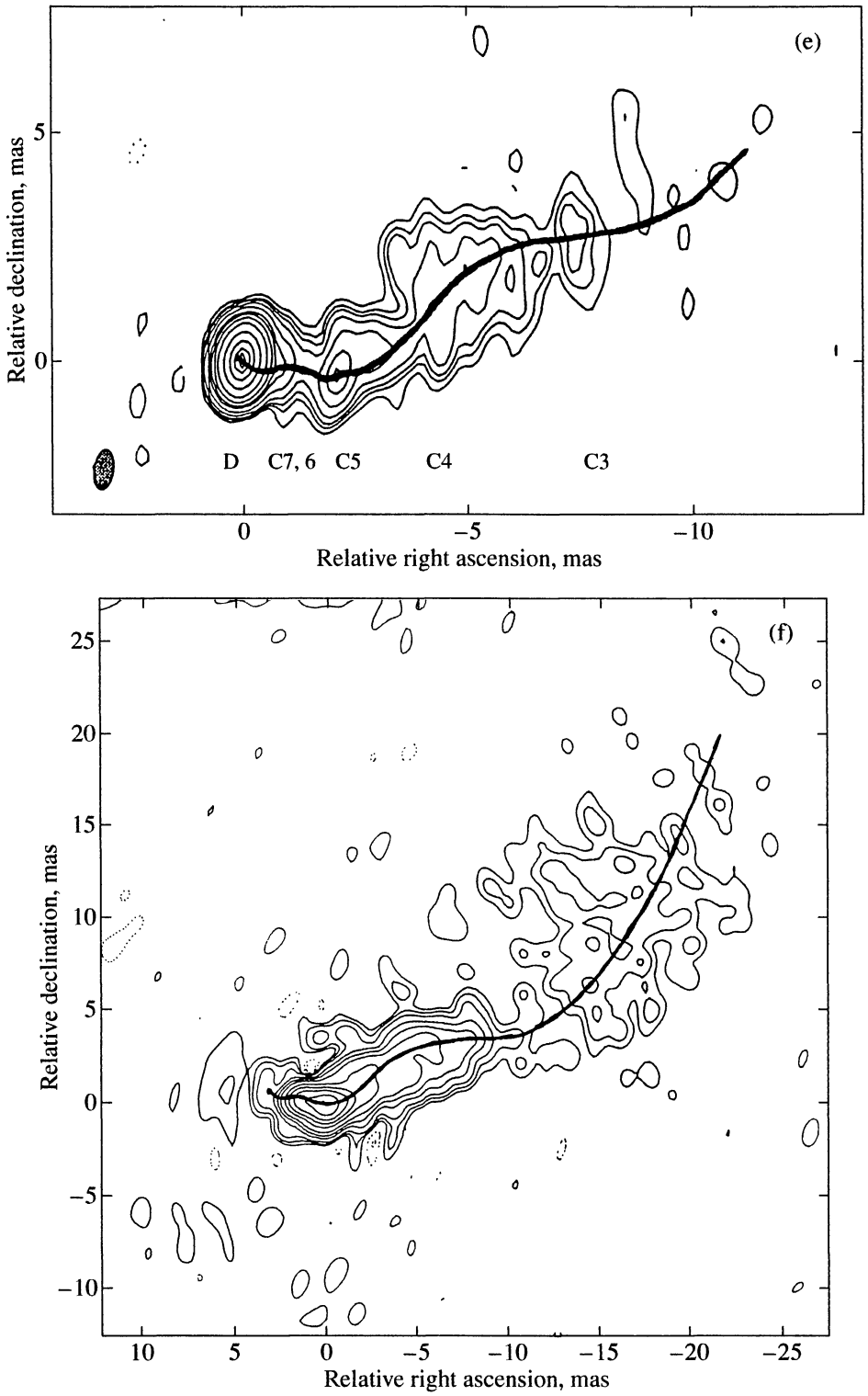

Fig. 1. (Contd.)

olution. We set it equal to 1×1 mas^2. The recalculated distributions of brightness, flux density per unit beam, $T_b(\rho) \sim F/\Omega$, along the helix are given in Table 1 and shown in Fig. 3.

As we see from the figures and Table 1, the peak brightness of the compact source, the injector ($\rho \approx 0$), is observed only at the shortest centimeter wavelengths (81.8 Jy beam^{-1} at 1.35 cm and 17.3 Jy beam^{-1} at

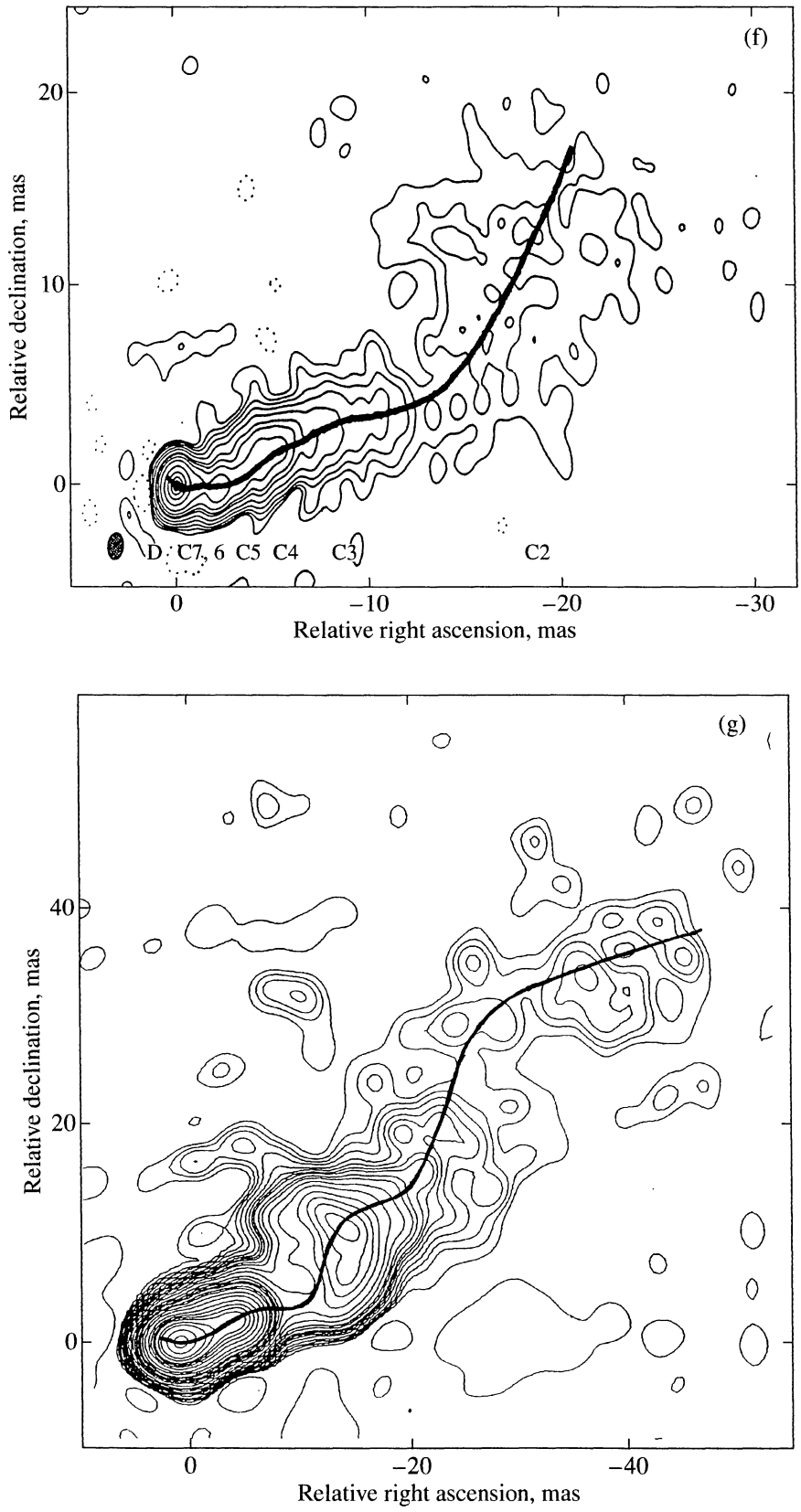

Fig. 1. (Contd.)

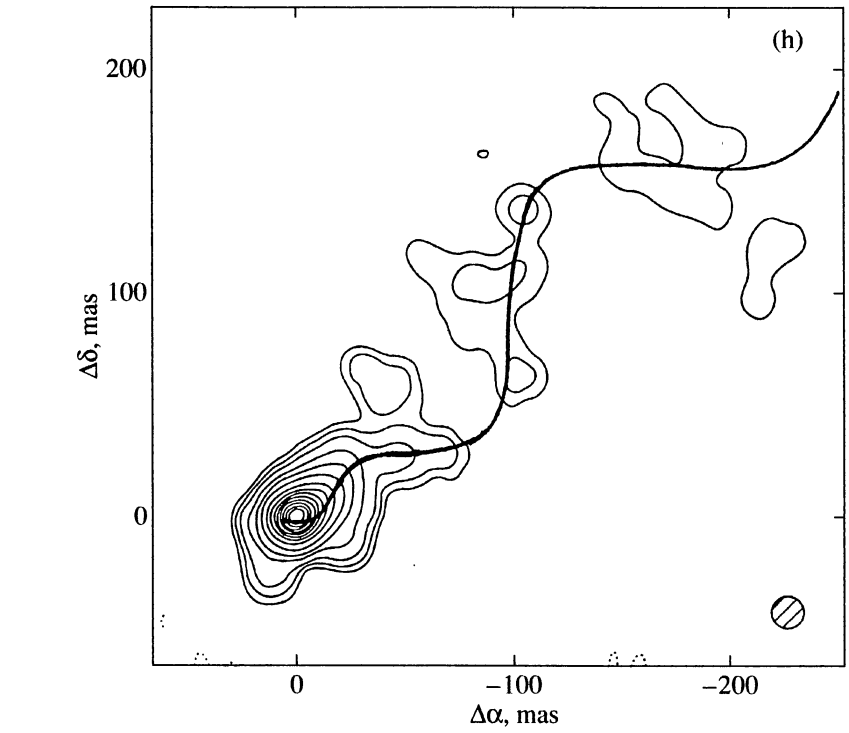

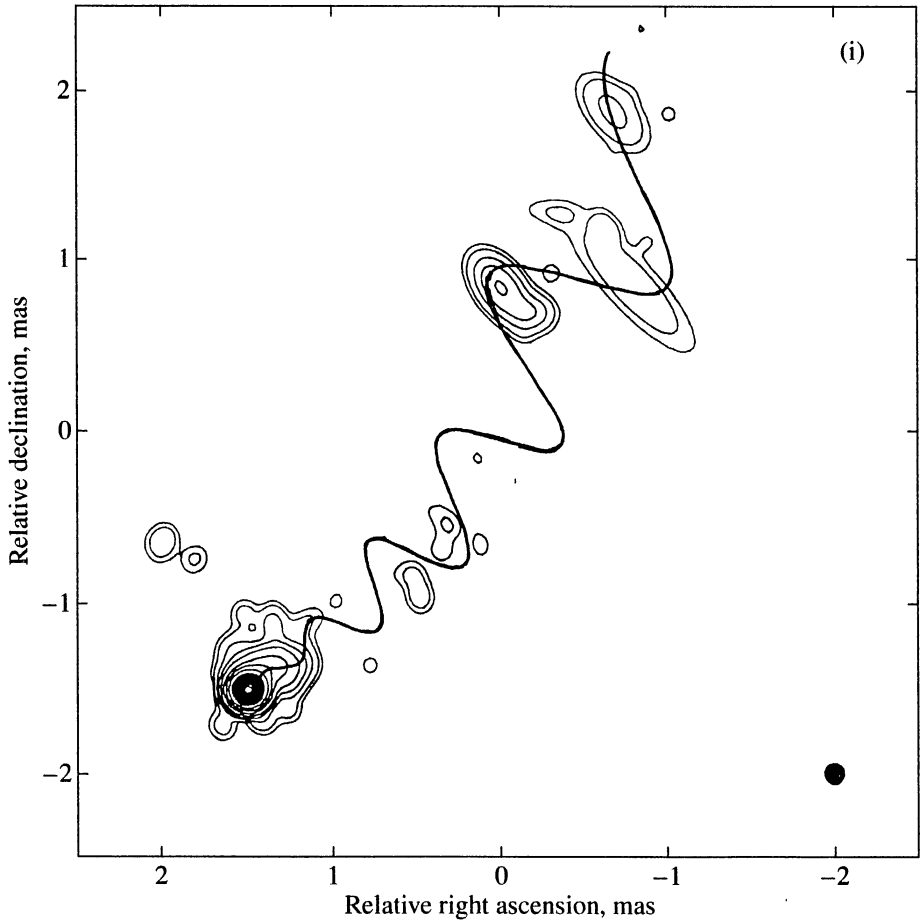

Fig. 1. (Contd.)

3.6 cm). The synchrotron radiation of the injector, the injected relativistic plasma, approaches the limiting brightness temperature $T_b = 10^{12}$ K. Brightness temperatures $T_b \approx 10^{11}$ K are observed at centimeter wavelengths in the adjacent parts of the jet at $\rho \leq 2$ mas. At decimeter wavelengths, the 18- and 49-cm emission from the nucleus and from the adjacent part of the jet is weakened significantly.

The brightness decline near the injector at decimeter wavelengths is attributable to absorption in the surrounding ionized medium (thermal plasma). The absorption by the ambient medium increases with wavelength, but the optical depth of the thermal plasma decreases with distance from the nucleus. For this reason, the brightness begins to rise at low frequencies at $\rho > 3$ mas. The peak-brightness region at 49 cm lies at a distance of 17 mas from the nucleus and has a brightness temperature that is also close to a limiting value of $T_b \approx 0.5 \times 10^{12}$ K. The further decrease in brightness temperature at large distances is attributable to a decrease in the optical depth of the jet relativistic plasma. The jet brightness temperature at low frequencies decreases from $T_b \approx 10^{10}$ K at ~30 mas to ~10^7 K at 1″–4″ mas.

The observed brightness variation along the helix at different frequencies reflects the variation in spectral index. Since the brightness distributions under consideration were obtained with different radiointerferometric arrays and at different wavelengths, they may have different systematic errors. However, even measurements at a single wavelength, for example, at 6 cm, show that the brightness distributions in the nuclear region which were obtained under identical conditions but at different epochs (1990.18 and 1992.51) can differ markedly from each other. This difference reflects the actual variations which are caused by the active processes that took place during this period (Figs. 1e and 1f). However, despite these constraints, we can nevertheless estimate the spectral indices and determine their dependence on distance from the nucleus. Based on the brightness distribution in Fig. 3 and Table 1, we calculated the spectral indices along the helix in various radio wavelength bands. The angular "resolution" is 1 mas[2]. Our results are presented in Table 2 and shown in Figs. 4a–4d. These figures correspond, respectively, to the "nucleus" spectrum and to the variation of the spectral index $\alpha(\rho)$ in the frequency range 8.4–22 GHz, in the ranges 5–8.4 GHz and 1.6–5 GHz, and in the range 0.6–1.6 GHz. The spectral indices at high frequencies and in distant parts of the jet correspond to optically thin sources of synchrotron radiation and lie in the range typical of them: $-1.3 < \alpha < -0.6$. Let us consider the distribution of spectral indices in more detail.

(i) The injector is the nearest part of the jet ($\rho <$ 1 mas). The radio flux density increases fairly steeply with frequency in the wavelength range 3.6–49 cm (f = 8.4–0.5 GHz) under consideration and corresponds

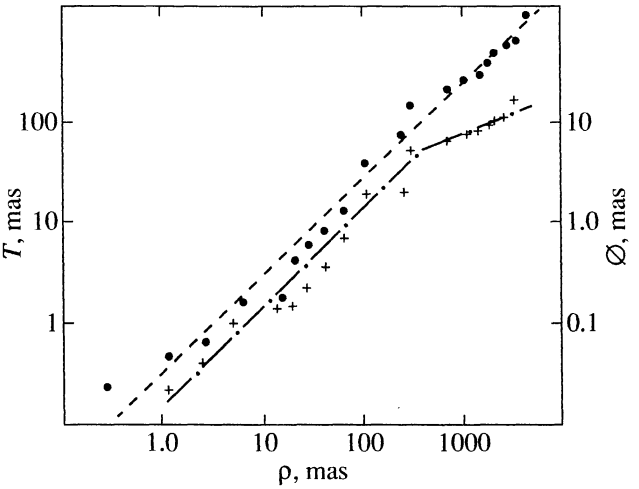

Fig. 2. Helix diameter (dashed line) and pitch (T) (dot-dashed line) versus distance from the injector.

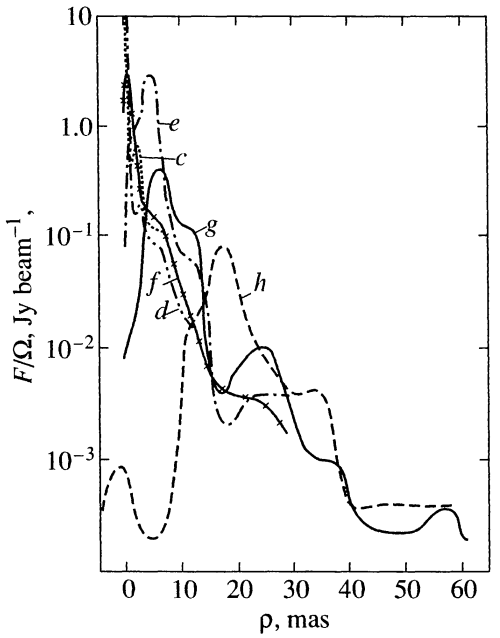

Fig. 3. Brightness distribution along the jet helix at various wavelengths (F/Ω = Jy beam^{-1}). The data were reduced to a 1-mas^2 beam: λ = 1.35 cm (c); λ = 3.6 cm (d); λ = 6 cm, epoch 1990 (e); λ = 6 cm, epoch 1992 (f); λ = 18 cm (g), and λ = 49 cm (h).

to the spectral index $\alpha = 4.0 \pm 0.2$. The spectrum flattens only when a wavelength of 1.35 cm is approached (Fig. 4a). This spectrum corresponds to a source of synchrotron radiation with a large optical depth $\tau > 1$ in the entire frequency range under consideration whose radio emission is appreciably absorbed by the thermal plasma.

(ii) At distances $1 < \rho < 3$ mas, the cutoff in the spectrum shifts to the frequencies 5–8.4 GHz. The spectral

Table 1. Radio flux density distribution at various wavelengths along the jet helix axis, in units of F/Ω (Jy beam^{-1}) (upper row) and the data reduced to a 1-mas^2 beam (lower row). K is the normalization coefficient

No.	ρ, cm	0	1	2	3	4	5	6
1	λ = 1.35 cm							
2	Ω = 0.35 × 0.17	4.9	0.025	0.04	0.02	≤0.01	≤0.01	0.01
3	K = 16.7	81.8	0.42	0.67	0.34	0.125	0.117	0.112
4	λ = 3.6							
5	Ω = 0.89 × 0.45	6.9	0.138	0.069	0.069	0.035	0.035	0.035
6	K = 2.5	17.3	0.40	0.20	0.25	0.12	0.11	0.11
7	λ = 6.0							
8	Ω = 1.43 × 0.83	3.0	–	0.3	–	0.15	–	0.15
9	K = 0.84	2.5	–	0.25	–	0.13	–	0.13
10	Ω = 1.0 × 1.0	0.08	–	1.0	–	2.9	–	1.0
11	λ = 18							
12	Ω = 3.0 × 3.0	0.08	–	0.2	–	2.0	–	3.6
13	K = 0.11	0.009	–	0.022	–	0.22	–	0.4
14	λ = 49							
15	Ω = 5.0 × 5.0	0.02	–	–	–	–	0.005	–
16	$K = 0.04 \times 10^3$	0.8	–	–	–	–	0.2	–

No.	7	8	9	10	11	12	14	16
4								
5	0.21	0.014	0.014	0.007	0.007	–	–	–
6	0.053	0.035	0.035	0.017	0.018	–	–	–
7								
8	–	0.06	–	0.03	–	0.015	0.004	0.004
9	–	0.05	–	0.025	–	0.013	0.005	0.004
10	–	0.15	–	0.07	–	0.06	0.03	0.003
11								
12	–	2.0	–	1.2	–	1.0	0.16	0.04
13	–	0.22	–	0.13	–	0.11	0.017	0.0044
14								
15	–	–	–	0.104	–	–	1.04	–
16	–	–	–	4.2	–	–	25.0	–

No.	18	20	22	24	26	28	30	32	34
7									
8	0.004	0.004	0.004	0.004	0.004	0.002	–	–	–
9	0.0034	0.0034	0.0034	0.0034	0.0025	0.002	–	–	–
10	0.002	0.002	0.004	0.004	0.004	0.004	–	–	–
11									
12	0.04	0.06	0.08	0.1	0.08	0.04	0.02	0.012	0.009
13	0.0044	0.007	0.009	0.01	0.009	0.004	0.002	0.001	0.001
14									
15	–	0.828	–	–	0.207	–	0.104	–	–
16	–	33	–	–	8.3	–	4.2	–	–

No.	35	36	38	40	42	44	46	48	50
11									
12		0.009	0.008	0.004	0.003	0.002	0.002	0.003	0.002
13		0.001	0.0009	0.00044	0.0003	0.0002	0.0002	0.0003	0.0002
14									
15	0.104	–	–	0.01	–	0.01	–	–	0.01
16	4.2	–	–	0.4	–	0.4	–	–	0.4

No.	52	54	56	58	60	62	64	66
11								
12	0.002	0.003	0.003	0.004	0.002	0.002	0.002	0.003
13	0.0002	0.0003	0.0004	0.0007	0.0002	0.0002	0.0002	0.0003
14								
15	–	–	0.01	–	–	–	–	–
16	–	–	0.4	–	–	–	–	–

Table 2a. Distribution of spectral indices $\alpha(\rho)$, $F = f^{\lambda}$, α — in the wavelength range $\Delta\lambda$ = 1.3–3.6 GHz, α_a — $\Delta\lambda$ = 3.6–6.0 cm, epoch Oct. 8, 1990 and α_b epoch June 4, 1992

ρ	0	1	2	3	4	5	6	8	10	Δλ
α	1.6	0.05	1.27	0.32	0.05	0.07	−0.02	–	–	1.3–3.6
α_a	3.27	–	−0.38	–	−0.12	–	−0.27	−0.62	−0.66	3.6–6.0
α_b	9.1		−2.72		−5.36		−3.73	−2.49	−2.41	3.6–6.0

Table 2b

ρ	0	2	4	6	8	10	12	14	16	18	20	22	24	26	28	Δλ
α_a	5.2	2.3	−0.5	−1.1	−1.4	−1.5	−2.0	−1.1	−0.1	−0.2	−0.7	−0.9	−1.0	−1.2	−0.6	6–18
α_b	2.0	3.6	2.4	0.9	−0.3	−0.6	−0.6	−0.5	−0.4	−0.7	−1.2	−0.8	−0.9	−0.8	0.0	6–18

Table 2c

ρ	0	5	10	14	20	26	30	35	40	45	50	55	Δλ
α	2.5	7.8	3.5	−0.4	−1.6	0.1	−0.8	−1.5	0.1	−0.7	−0.7	0	18–49

index is $\alpha = -0.2 \pm 0.2$ in the high-frequency part and α = (3.5–4) in the low-frequency part at decimeter wavelengths (Fig. 4b). In the frequency range 8.4–22 GHz, the spectral index is $\alpha = 1.3 \pm 0.2$ at ρ = 2 mas and decreases to zero at 6 mas. The observed spectral indices in these regions correspond to individual dense components (Fig. 1c).

(iii) The same shape of the spectrum with a low-frequency cutoff is preserved up to ρ = 12 mas from the nucleus; the cutoff continues to shift to lower frequencies. The spectral index at ρ = (12–50 mas) varies in the range α = –(0.7–1.3) (Fig. 4d). These variations are attributable to individual local structures. At points of peak brightness at 49 cm (ρ = 20 and 35 mas), the spectrum steepens and the spectral index is α = –1.5. The spectral index is α = –0.8 at large distances $\rho \sim (1''–1''.5)$ in the wavelength range λ = 6–18 cm and α = –1.6 at distances ρ = (2″–4″) from the nucleus at wavelengths 6–74 cm.

The above analysis shows that the spectrum of the region near the injector has a low-frequency cutoff with the spectral index $\alpha = 4 \pm 0.2$ at frequencies $f \leq 10$ GHz. Positive spectral indices in this region at centimeter wavelengths were also obtained by Zensus *et al.* (1993). In the limiting case, the spectral index of an optically thick source of synchrotron radiation can reach α = 2.5; actually, it does not exceed 2 (Kellermann 1974a). The fact that the observed spectral index exceeds this limit suggests that the synchrotron radiation is absorbed by the external ionized medium. A similar conclusion also follows from the anticorrelation between high-frequency and low-frequency bursts. There is no correlation between the low-frequency variations in nearby AGNs, including the quasar 3C 345.

The low-frequency variability of 3C 345 was found to be caused by the change in the size of a bright emitting region ~5 mas in size (Fig. 2h). For 1983.9–1990.8 (λ = 49 cm), the angular size of this region approximately doubled, but its brightness temperature was essentially constant: $T_b \approx 0.6 \times 10^{12}$ K. The brightness temperature of the nucleus itself is considerably lower, which is attributable to absorption in the surrounding thermal plasma.

The nuclear regions of AGNs are surrounded by an ionized medium that emits emission lines, which are used to determine the redshifts. The electron density in the narrow-emission-line region is $N_e = 10^{(4-6)}$ cm^{-3} (Netzer 1987), and its extent is $l \sim 10^{20}$ cm (33 pc) or ~8 mas for the quasar 3C 345. The broad emission lines originate in a more compact region ~10^{18} cm in size with a higher electron density ~10^{10} cm^{-3}. Thus, the presence of a fairly dense, ionized medium which obscures the nuclear region follows from independent optical data; its extent is in agreement with radio-astronomical data.

The absorption by an ionized medium e^{τ} is determined by its optical depth

$$\tau = 0.08\, T_e^{-1.35}(1+z)^{-2.1} f^{-2.1}\,\mathrm{ME}, \qquad (1)$$

where $\mathrm{ME} = \int N_e^2 dl$ is the emission measure.

At λ = 49 cm, the optical depth of the screen for the objects under consideration is $\tau = 16 \times 10^{-8}$ ME. Based on the recombination time $t = 10^5/N_e$ years and on the time scale of the low-frequency variability $t \approx 1$ year (Padrielli 1982), we find the electron density in the absorbing screen to be $N_e \geq 10^5$ cm^{-3}. This value matches the electron density in the narrow-emission-line region. The part of the absorbing screen under consideration is in front of the observed bright region at 49 cm. The electron density in the screen increases as one approaches the nucleus. Based on the absorption,

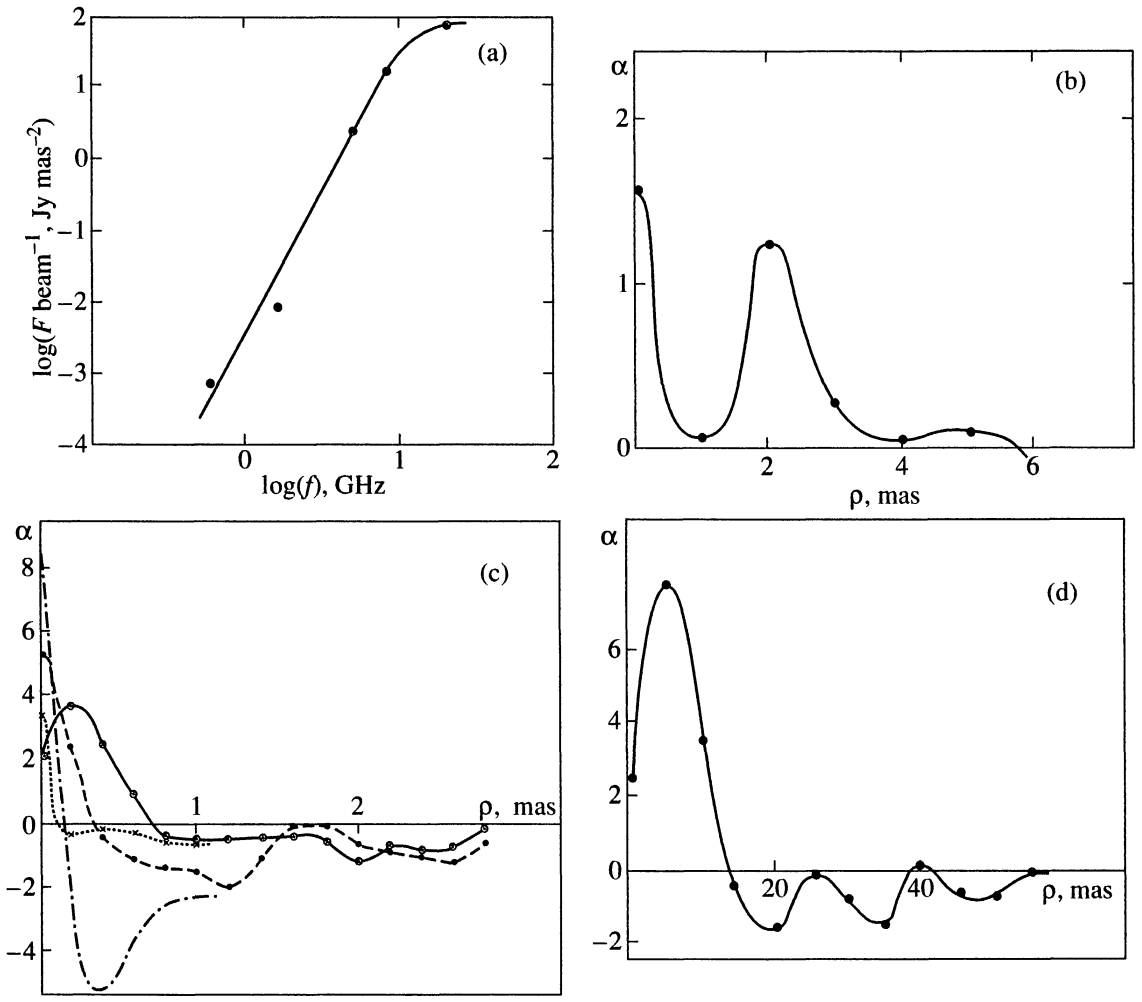

Fig. 4. (a) Radio spectrum for the injector region in the quasar 3C 345; the spectral-index distribution along the helix in the wavelength range (1.3–3.6 cm) (b); in the range (3.6–6) cm, the dot-dashed line for Oct. 8, 1990, the dotted line for June 4, 1992 (c); in the range (6–18) cm, the solid line for Oct. 8, 1990, the dashed line for June 4, 1992 (c); and in the range (18–49) cm (d).

we find the optical depth of the screen near the injector at $\lambda = 49$ cm to be $\tau \approx 6$. For the electron density $N_e = 10^{5-6}$ cm^{-3} in this region, the thickness of the screen wall does not exceed $l < 10^{-3}$ pc. Even if the thickness of the cocoon wall slightly increases with distance from the nucleus, its thickness does not constrain the observed time scale of the low-frequency variability: $l/c \ll 1$ year.

Thus, the starting part of the jet is cocooned in a thin layer of ionized gas. The thickness of the cocoon wall and the particle density are determined by equilibrium between the thermal- and relativistic-plasma pressures. The pressure in the jet is proportional to the particle density squared and decreases with distance as $P_j \sim (\rho_0/\rho)^2$ (Begelmann *et al.* 1984). In this case, $N_e \sim (\rho_0/\rho)^2$, while the wall thickness is proportional to ρ and its optical depth; accordingly, its emission measure is $\sim\rho^{-3}$.

The ionized medium of the cocoon wall affects polarization characteristics of the recorded radio emission. The compact bright components at high frequencies are observed within 6 mas of the injector. The transparency of the cocoon wall varies with time and increases with distance from the nucleus. The wall is virtually transparent at millimeter and short centimeter wavelengths. However, it affects the polarized emission (Matveenko *et al.* 1996). For example, during 1980–1993, the emission at $\lambda = 6$ cm exhibited variations in intensity, which were also accompanied by variations in polarization (Browne *et al.* 1994). The polarized emission increased in intensity simultaneously with the total emission. However, having reached a certain level, it began to decrease, while the total emission continued to increase in intensity: the degree of polarization decreased. During the decline, the variations occurred in the reverse order. The polarized emission increased in intensity with distance from the nucleus and reached

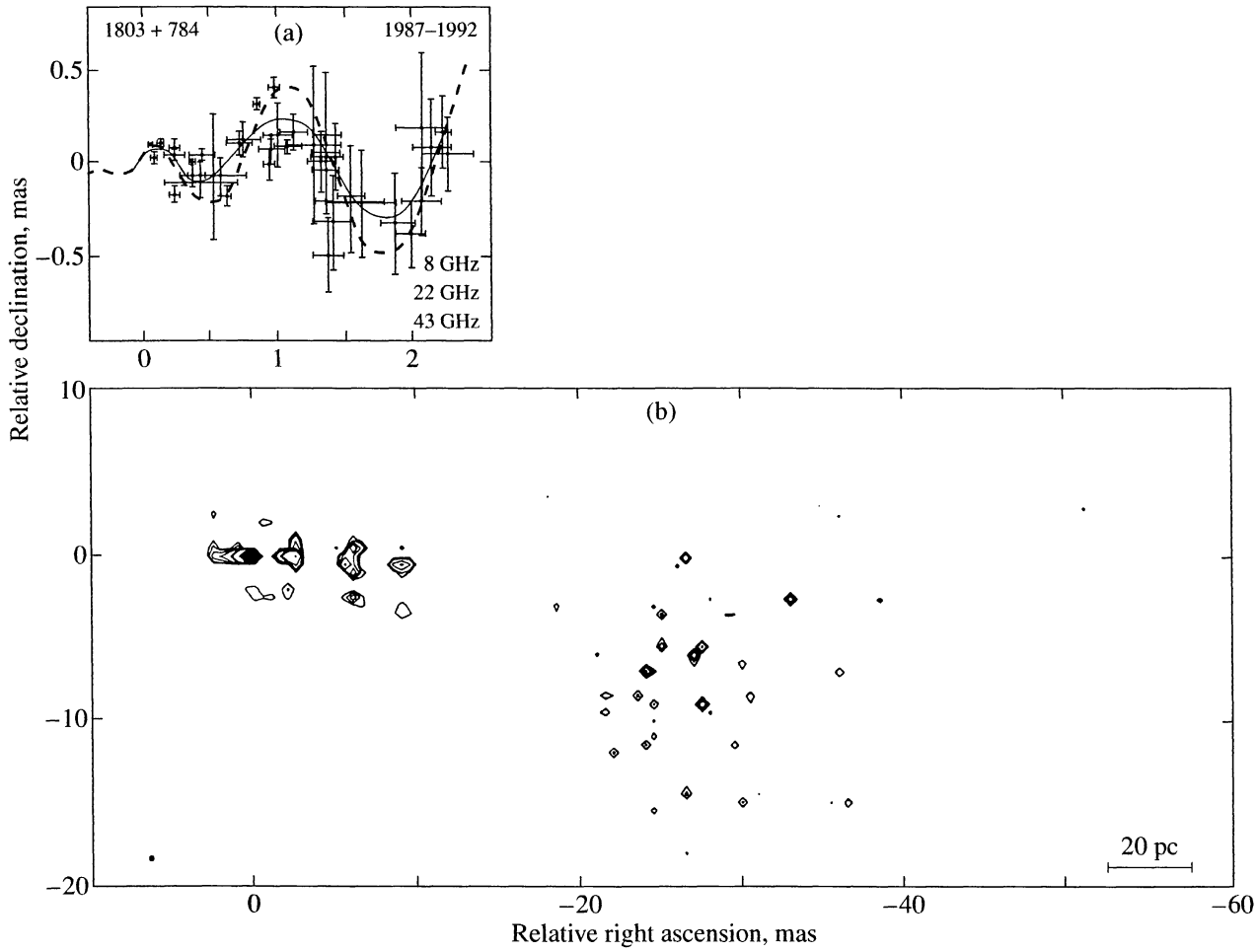

Fig. 5 (a) Trajectory of the compact components (Krichbaum *et al.* 1993). (b) Image of the quasar 1803+784 at $\lambda = 18$ cm, epoch 1993.41, the isophotal levels are (0.07, 0.15, 0.30, 0.50, 1.0, 2.0, 5.0, 10.0, 15.0, 20.0, 30.0, 50.0, 70.0, 90.0)%; the peak brightness is 1.129 Jy beam^{-1}; a 0.3 × 0.3-mas^2 beam.

a peak at ~4.5 mas. The rotation measure as inferred from low-angular-resolution measurements in the wavelength range $\lambda = 18$–21 cm is RM ≈ 29 rd m^{-2}, and the degree of polarization is $P \approx 4\%$ (Rudnick and Jones 1983). This rotation measure must be attributed to the region behind the observed peak emission at 6 cm rather than to the nucleus. The position angle of the polarization plane at 6 cm corrected for Faraday rotation is PA = –70° and matches the position angle of the jet at this place. For a large optical depth, the degree of polarization is $P_0 \leq 10\%$, and the polarization plane is parallel to the magnetic field (Kellermann 1974b). Since the region under study is optically thick, the magnetic field of the jet at this place (~7 mas from the nucleus) is aligned with its axis. At the same time, the longitudinal magnetic-field component in the cocoon wall is $B_\parallel = 0.5$ μG and decreases as $\sim(\rho/\rho_0)^{-2}$, while the rotation measure is $\sim (\rho/\rho_0)^{-3}$. The rotation measure in the nuclear region reaches RM = 8 × 10^4 rad m^{-2}, the electron density is $N_e = 10^6$ cm^{-3}, and the magnetic field is $B_\parallel = 0.1$ mG. The observed degree of polarization depends on signal reception band and on rotation measure. For the above rotation measure and signal reception band (28 MHz), the degree of polarization must decrease by approximately a factor of 4 at 6 cm (Matveenko *et al.* 1996), which is confirmed by observations.

THE BL Lac OBJECT 1803+784

This object is similar in properties to the quasar 3C 345. Ejections of compact objects in directions PA ≈ –(68–110)° are observed in its nuclear region at millimeter wavelengths. The components' motion is traceable up to distances of 0.1–25 mas from the nucleus. The injection cone angle is ~40°, and the cone axial orientation is 90°. The components move along a divergent conical helical trajectory (Krichbaum *et al.* 1993). The cone angle is 34° (Fig. 5a). The diameter of

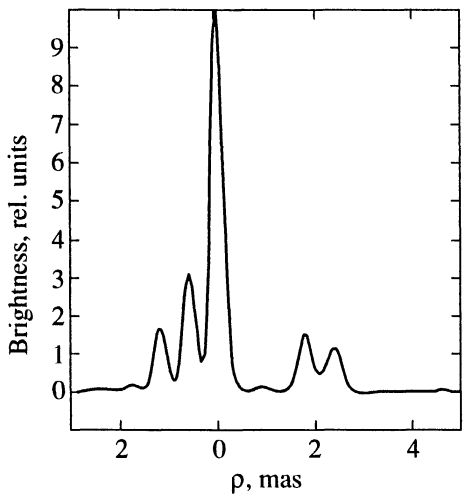

Fig. 6. Brightness profile along the jet axis in the object 1803+784 at λ = 18 cm, the beam is 0.3 × 3.0 mas^2, the peak brightness is 3.54 Jy beam^{-2}, and the total radio flux is 2.74 Jy.

the helix increases with distance ρ from the nucleus as ∅ = 0.6ρ, and its pitch is $T \approx \rho$.

Observations with a global radiointerferometric array at 18 cm in a wide dynamic range indicate that the brightness distribution in the jet has the shape of a cone and is divided into two parts (Britzel *et al.*, in preparation). Figure 5a shows a synthesized image of the object in the form of "points" 0.3 mas in size. The points concentrate in two regions which are spaced 25 mas apart and are distributed in a 23° cone. The cone axis is curved. The position angle of the cone (in degrees) varies with distance ρ as PA = –(90 + 1.5ρ).

As we see from the figure, the part of the jet that is adjacent to the injector consists of a thin jet and several compact components. The intensity of the brightest component is 3.54 Jy beam^{-1}. It would be reasonable to assume that the injector lies at the cone base. In this case, the radio emission from nearby components is greatly weakened. Their minimum brightness is traceable up to <0.07% of the peak value. Figure 6 shows the brightness profile along the jet axis with a 0.3 × 3.0 mas^2 knife beam oriented at PA = –10°. The nucleus lies at 2.8–3 mas from the component with peak brightness; its brightness is <25 db of this value. The brightness of the structure increases with distance from the nucleus, which can be explained by the increase in the transparency of the ambient ionized medium. The change in brightness is essentially exponential. It thus follows that the optical depth of the absorbing screen at ρ ≤ 3 mas varies linearly and can be represented as

$$\tau = \tau_0(1 - \rho/\rho_0),$$

where $\tau_0 = 5.5$ is the optical depth in the injector (nuclear) region and $\rho_0 = 3$ mas.

Based on the low-frequency variability of the brightest component with t = 1.5–2 years (Aller and Aller 1982) and on its recombination time, we find the thermal-plasma electron density in the region of its location to be $N_e \geq 0.5 \times 10^5$ cm^{-3}. The low-frequency variability must be associated with the region of dominant radio emission at 3 mas from the nucleus. The thickness of the screen (cocoon) wall in the region of peak brightness (l) can be determined from its optical depth. For an optical depth $\tau \sim 1$ and for the above electron density, the screen thickness does not exceed $l < 10^{-2}$ pc. Such a small thickness of the cocoon wall is not a limiting factor for the time scale of the low-frequency variability. A change in electron density of $N_e \sim 10\%$ is enough to account for the observed low-frequency variability. A linear decrease in the optical depth of the screen with distance from the nucleus corresponds to a similar change in emission measure and electron density $N_e \sim \rho^{-2}$.

The polarization of 1803+784 at 18–21 cm is P = 3.9%, and its position angle is PA = –129°. The rotation measure is RM = –62 rad m^{-2}. The polarization was assumed to be determined by the emission from the nucleus (Wrobel *et al.* 1987). The rotation measure of nearby radio sources is RM ≈ 20 rad m^{-2} and matches the Galactic rotation measure in the this direction. It would be reasonable to assume that the interstellar medium also affects the object under study. In this case, the rotation measure of the object 1803+784 itself, corrected for the Galactic rotation measure, is RM ≈ –80 rad m^{-2}. This rotation measure must be attributed to its brightest region at ρ ≈ 3 mas from the injector rather than to the nucleus. The polarization at 3.6 cm is P = (15–20%) and is determined by the nuclear region; the position angle of the polarized emission is PA = 90° and matches that of the jet.

The degree of polarization depends on the optical depth of the emitting region. An optically thin region can have $P_0 \leq 70\%$; the (polarization) electric vector E in this case is perpendicular to the magnetic field. For a large optical depth, $P_0 \leq 10\%$ and E is parallel to the magnetic field B (Kellermann 1974b). At 3.6 cm, the observed degree of polarization is P = 20% and the brightness temperature is $T_b < 10^{12}$ K, which corresponds to a source with a sufficiently large optical depth. In this case, the magnetic field of the jet near the injector is parallel to its axis.

The observed emission at 18 cm also originates from the optically thick source, as confirmed by its high brightness temperature ($T_b \approx 10^{12}$ K), and E must be parallel to the magnetic field B. Thus, the magnetic field is also parallel to the jet axis at 3 mas from the injector.

The parameters of the cocoon wall, as inferred from 18 cm observations at R = 2.8 mas from the nucleus, are $N_e \sim 10^5$ cm^{-3} and $l = 10^{-2}$ pc. These data and the rotation measure RM = $8.1 \times 10^5 N_e B l$ rad m^{-2} can be used to determine the longitudinal magnetic-field compo-

nent in the cocoon wall. For RM = 80 rad m^{-2}, the magnetic field is $B_{\parallel} \approx 0.1$ μG.

CONCLUSION

The sources 3C 345 and 1803+784 are typical representatives of objects with active galactic nuclei and one-sided jets. Their compact components move along conical helical trajectories. The helix diameter and pitch are proportional to the distance from the injector. The helix axes are curved. This structure can be explained by a multimode precession of the accretion-disk (injector) rotation axis. The rotation period of the accretion disk is 14 rotations per year.

The high-velocity precession of the rotation axis of the quasar 3C 345 corresponds to one rotation in seven years, and the precession angle is 60°. The low-velocity precession determines an ~75° bending of the jet in its lifetime of ~10^6 years. The helical structure of the jet is an extension of the trajectory along which the compact components move.

The nucleus corresponds to the exit part of the injector, the starting part of the jet. The radio brightness temperature of the nucleus and of the adjacent part of the jet matches the Compton limit $T_b \approx 10^{12}$ K.

The jet is cocooned in a thin layer of thermal plasma. The cocoon electron density in the injector region is $N_e \sim 10^6$ cm^{-3} and decreases with distance as $\sim\rho^{-2}$. The wall thickness is $<10^{-2}$ pc and increases with distance from the nucleus as ~ρ. The longitudinal magnetic-field component in the cocoon wall in the part which is adjacent to the nucleus is $B \sim 0.1$ mG.

Absorption in the cocoon wall restricts the visibility of the nuclear region at low frequencies, which determines the low-frequency cutoff in the spectrum; the cutoff frequency lies at short centimeter wavelengths. As one recedes from the injector, the cutoff frequency shifts to decimeter waves. The high-frequency spectral index lies in the range $\alpha = -(0.8–1.6)$. The change in wall transparency causes the low-frequency variability of the quasar and determines the observed variations in the polarization characteristics of the emission at high frequencies.

The polarization plane of the jet synchrotron radiation in the part which is adjacent to the injector is parallel to the jet axis. The optical depth of the emitting region is large enough, suggesting that the magnetic field of the jet is parallel to its axis.

The object 1803+784 has a cone-shaped jet. The 18-cm emission from the injector region is appreciably weakened, by a factor of ~300. The parameters of the cocoon wall are similar to those for the quasar 3C 345.

ACKNOWLEDGMENTS

L.I. Matvyenko wishes to thank the Max-Planck-Institut für Radioastronomie (MPIFR) and the Joint European Radiointerferometry Institute (JIVE) for support of these studies.

REFERENCES

Aller, H.D. and Aller, M.F., Low Frequency Variability of Extragalactic Radio Sources, Proc. NRAO Workshop, Cotton, W.D. and Spangler, S.R., Eds., *Publ. Nat. Radio Astron. Obs.*, 1982, p. 185.

Bååth, L.B., Rogers, A.E.E., Inoue, M., *et al.*, *Astron. Astrophys.*, 1992, vol. 257, p. 31.

Begelmann, M.C., Blanford, R.D., and Rees, M.J., *Rev. Mod. Phys.*, 1984, vol. 56, p. 255.

Biretta, J.A., Moore, R.L., and Cohen, M.H., *Astrophys. J.*, 1986, vol. 308, p. 93.

Bisnovatyi-Kogan, G.S., Kogan, B.M., and Fridman, A.M., *Astron. Zh.*, 1969, vol. 46, p. 369.

Bregman, J.N., Glassgold, A.E., Huggins, P.J., *et al.*, *Astrophys. J.*, 1986, vol. 301, p. 708.

Browne, I.W.A., Orr, M.J.L., Davis, R.J., *et al.*, *Mon. Not. R. Astron. Soc.*, 1982, vol. 198, p. 673.

Browne, L.F., Roberts, D.H., and Wardle, J.F.C., *Astrophys. J.*, 1994, vol. 437, p. 108.

Cohen, M.H., Moffet, A.T., Romney, J.D., *et al.*, *Astrophys. J.*, 1976, vol. 206, p. L1.

Gopal-Krishna, Singal, A.K., and Krishnamohan, S., *Astron. Astrophys.*, 1984, vol. 140, p. L19.

Kellermann, K.I. and Pauliny-Toth, I.I.K., *Ann. Rev. Astron. Astrophys.*, 1981, vol. 19, p. 373.

Kellermann, K.I. and Pauliny-Toth, I.I.K., *Astrophys. J.*, 1969, vol. 155, p. L31.

Kellermann, K.I., *Galactic and Extragalactic Radio Astronomy*, Verschuur, G.L. and Kellermann, K.I., Eds., Berlin: Springer, 1974b, p. 346.

Kellermann, K.I., *Galactic and Extragalactic Radio Astronomy*, Verschuur, G.L. and Kellermann, K.I., Eds., Berlin: Springer, 1974a, p. 342.

Krichbaum, T.P., Witzel, A., and Graham, D.A., *et al.*, *Astron. Astrophys.*, 1993, vol. 275, p. 375.

Lobanov, A.P. and Zensus, J.A., *Extragalactic Radio Sources—From Beam to Jets*, Roland, J., Sol, H., and Pelletier, G., Eds., 1991, p. 157.

Lobanov, A.P., Zensus, J.A., and Leppanen, K.J., *Bull. Am. Astron. Soc.*, 1993, vol. 25, p. 1382.

Lovelace, R.V., Berk, H.L., and Contopoulos, J., *Astrophys. J.*, 1991, vol. 379, p. 696.

Matveenko, L.I. and Pauliny-Toth, I.I.K., Bååth, L.B., *et al.*, *Astron. Astrophys.*, 1996, vol. 312, p. 738.

Matveenko, L.I., Graham, D.A., and Pauliny-Toth, I.I.K., *et al.*, *Pis'ma Astron. Zh.*, 1992, vol. 18, p. 931. *Sov. Astron. Lett.*, 1992, vol. 18, p. 379.

Netzer, H., *Astrophysical Jets and Their Engines*, Kundt, W., Ed., Dordrecht: D. Reidel, 1987, p. 103.

Padrielli, L., Low Frequency Variability of Extragalactic Radio Sources, Proc. NRAO Workshop, Cotton, W.D. and Spangler, S.R., Eds, *Publ. Nat. Radio Astron. Obs.*, 1982, part 1.

Rantakyrö, F.T., Bååth, L.B., and Matveenko, L.I., *Astron. Astrophys.*, 1995, vol. 293, p. 44.

Rantakyrö, F.T., Bååth, L.B., Pauliny-Toth, I.I.K., *et al.*, *Astron. Astrophys.*, 1992, vol. 259, p. 8.

Readhead, A.C.S., Cohen, M.H., Perason, T.J., *et al.*, *Nature*, 1978, vol. 276, p. 768.

Rudnick, L. and Jones, T.W., *Astron. J.*, 1983, vol. 88, p. 518.

Shakura, N.I. and Sunyaev, R.A., *Astron. Astrophys.*, 1973, vol. 24, p. 337.

Unwin, S.C. and Wehrle, A.E., *Astrophys. J.*, 1992, vol. 398, p. 74.

Wrobel, J.M., Pearson, T.J., Cohen, M.H., *et al.*, *IAU Symp. no. 129: The Impact of VLBI on Astrophysics Geophysics*, Reid, M.J. and Moran, J.M., Eds., 1988, p. 165.

Zensus, J.A., *Extragalactic Radio Sources—From Beam to Jets*, Roland, J., Sol, H., and Pelletier, G., Eds., Cambridge Univ., 1991, p. 154.

Zensus, J.A., *Parsec Scale Radio Jets*, Zensus, J.A. and Pearson, T.J., Eds., Cambridge Univ., 1990, vol. 17, p. 28.

Zensus, J.A., Cohen, M.H., and Unwin, S.C., *Astrophys. J.*, 1995, vol. 443, p. 35.

Translated by V. Astakhov